Received: 12 August 2022 | Revised: 15 September 2022 | Accepted: 29 September 2022

DOI: 10.1002/cey2.297

RESEARCH ARTICLE

CARBON ENERGY WILEY

Large ferro–pyro–phototronic effect in $0.5Ba(Zr_{0.2}Ti_{0.8})O_3$–$0.5(Ba_{0.7}Ca_{0.3})TiO_3$ thin films integrated on silicon for photodetection

José P. B. Silva[1,2] | **Katarzyna Gwozdz**[3] | **Luís S. Marques**[1,2] | **Mario Pereira**[1,2] | **Maria J. M. Gomes**[1,2] | **Judith L. MacManus-Driscoll**[4] | **Robert L. Z. Hoye**[5,6]

[1]Centre of Physics of Universities of Minho and Porto (CF-UM-UP), University of Minho, Braga, Portugal

[2]Laboratory of Physics for Materials and Emergent Technologies, LapMET, University of Minho, Braga, Portugal

[3]Department of Quantum Technologies, Faculty of Fundamental Problems of Technology, Wroclaw University of Science and Technology, Wroclaw, Poland

[4]Department of Materials Science and Metallurgy, Cambridge, UK

[5]Inorganic Chemistry Laboratory, Department of Chemistry, University of Oxford, Oxford, UK

[6]Department of Materials, Imperial College London, London, UK

Correspondence

Judith L. MacManus-Driscoll, Department of Materials Science and Metallurgy, 27 Charles Babbage Rd., Cambridge CB3 OFS, UK.
Email: jld35@cam.ac.uk

José P. B. Silva, Centre of Physics of Universities of Minho and Porto (CF-UM-UP), University of Minho, Campus de Gualtar, Braga 4710-057, Portugal.
Email: josesilva@fisica.uminho.pt

Funding information

Royal Academy of Engineering, Grant/Award Number: RF\201718\1701; ERC grant, Grant/Award Number: EU-H2020-ERC-ADG # 882929; Portuguese Foundation for Science and Technology, Grant/Award Number: UIDB/04650/2020; Royal Academy of Engineering Chair in Emerging Technologies, Grant/Award Number: CIET1819_24; European Union's Horizon 2020 research and innovation programme, Grant/Award Number: 958174; EPSRC CAM-IES, Grant/Award Number: EP/P007767/

Abstract

Coupling together the ferroelectric, pyroelectric, and photovoltaic characteristics within a single material is a novel way to improve the performance of photodetectors. In this work, we take advantage of the triple multifunctionality shown by $0.5Ba(Zr_{0.2}Ti_{0.8})O_3$–$0.5(Ba_{0.7}Ca_{0.3})TiO_3$ (BCZT), as demonstrated in an Al/Si/SiO_x/BCZT/ITO thin-film device. The Si/SiO_x acts as an n-type layer to form a metal–ferroelectric–insulator–semiconductor heterostructure with the BCZT, and with Al and ITO as electrodes. The photo-response of the device, with excitation from a violet laser (405 nm wavelength), is carefully investigated, and it is shown that the photodetector performance is invariant with the chopper frequency owing to the pyro-phototronic effect, which corresponds to the coupling together of the pyroelectric and photovoltaic responses. However, the photodetector performance was significantly better than that of the devices operating based only on the pyro-phototronic effect by a factor of 4, due to the presence of ferroelectricity in the system. Thus, after a poling voltage of −15 V, for a laser power density of 230 mW/cm^2 and at a chopper frequency of 400 Hz, optimized responsivity, detectivity, and sensitivity values of 13.1 mA/W, 1.7×10^{10} Jones, and 26.9, respectively, are achieved. Furthermore, ultrafast rise and fall times of 2.4 and 1.5 μs, respectively, are obtained, which are 35,000 and 36,000 times faster rise and fall responses, respectively, than previous reports of devices with the ferro–pyro–phototronic effect. This is understood

based on the much faster ferroelectric switching in ferroelectric thin films owing to the predominant 180° domains in a single direction out of plane.

KEYWORDS
ferroelectric, ferro–pyro–phototronic effect, photodetector, polarization-controlled response

1 | INTRODUCTION

Ultraviolet (UV), visible (Vis), and near-infrared (NIR) photodetectors (PDs) are widely used in optoelectronics, such as light sensing, environmental monitoring, life sciences, and optical communication, among others.[1,2] In particular, the wide bandgap semiconductor-based PDs for the UV to visible wavelength range (UV-Vis) have shown the advantages of having a simple structure, facile miniaturization, and robustness against radiation in severe environments.[3] Moreover, the possibility of achieving a self-powered PD, which consumes low or even no power from external power sources, is attracting tremendous attention for the next generation of optoelectronic devices.[4]

Nowadays, the self-powered PDs that are being investigated for UV-Vis are mainly based on semiconductors, such as ZnO and its heterostructures.[4] It was proposed that the light-induced pyroelectric effect in zinc oxide (ZnO) nanowires (NWs) could significantly improve the performance of PDs, based on the so-called pyro–phototronic effect.[5] This effect corresponds to the coupling of the light-induced pyroelectric effect, photonic excitations, and semiconductor properties, and can be used as an effective approach to enhance the performance of self-powered PDs from the UV to NIR.[6] Owing to its wide bandgap (3.37 eV), high exciton binding energy (ca. 60 meV), strong absorption in the UV range, and tunable electronic properties, ZnO is one of the most promising materials for self-powered PDs.[5,7] However, ZnO has a low pyroelectric coefficient of only around 1.5 nC/cm^{2}K,[8] and this limits the performance of the PDs. Therefore, it is necessary to exploit other pyroelectric materials for enabling the next generation of high-performance PDs based on the pyro–phototronic effect.

In this context, lead-free pyroelectric and ferroelectric oxide materials, such as $BaTiO_3$ (BTO), have emerged as promising candidates for self-powered visible PD devices based on multifunctional coupling of two or more of degrees of freedom of pressure, temperature, and light.[9] Indeed, Yang and co-workers investigated the ferro–pyro–phototronic effect in BTO ceramics[10,11] and proposed that the change of spontaneous polarization derived from light-induced thermal fluctuations can effectively modulate the carrier generation, separation, transportation, and recombination at the interface of the junctions and therefore enhance the PD performance. The triple functional effect has also been shown in $Bi_{0.5}Na_{0.5}TiO_3$ (BNT) ceramics.[12] Here, the photoresponse current was increased upon violet illumination by 131% (photovoltaic effect) and then by a further 57% upon heating (pyroelectric coefficient), with the increase linked also to the photoexcited carrier concentration and carrier mobility increasing with the temperature. However, the devices had very slow rise (τ_r) and fall times (τ_f) of 84.2 and 54.4 ms, respectively.

When compared with lead-free $BaTiO_3$ and $Bi_{0.5}Na_{0.5}TiO_3$ ceramics, $0.5Ba(Zr_{0.2}Ti0_{0.8})O_3$–$0.5(Ba_{0.7}Ca_{0.3})TiO_3$ (BCZT) ceramics show a higher pyroelectric coefficient of 5.0×10^{-4} C/m^{2}K,[13] cf. 16 nC/cm^{2}K ($BaTiO_3$), and ~50 nC/cm^{2}K ($Bi_{0.5}Na_{0.5}TiO_3$),[8,12] which makes BCZT more promising for PDs. Compared to ceramics, thin films should have a much larger light-induced temperature gradient (higher by a factor of the thickness ratio [>10^2]). The ferroelectric switching should also be faster because of the predominance of 180° domains.[14] Understanding the polarization switching mechanism in ferroelectric thin films is important for controlling their behavior. While the Kolmogorov–Avrami–Ishibashi (KAI) model describes the polarization reversal behavior of many single crystals,[15] Tagantsev et al.[16] proposed the nucleation-limited switching (NLS) model as an alternative approach to the KAI model to explain the polarization reversal kinetics. This model is based on the statistics of nucleation and growth of the reversed domains and was previously proposed to explain the switching dynamics in BCZT films, with the ferroelectric switching occurring in the ns range in BCZT thin films,[15] while in BCZT ceramics, it is one order of magnitude higher.[17] However, Swain et al. investigated the PD characteristics of Au/BCZT (700 nm)/Pt devices by using a Xenon arc lamp as the light source. The PD showed a poor responsivity of 0.25 mA/W and a low detectivity of 2.4×10^9 Jones.[18] There was no practical information on fall and rise times, or the sensitivity of the PDs.

In the present work, a novel thin-film device of Al/Si/SiO_x/BCZT/ITO was investigated and the photoresponse to illumination with a 405 nm wavelength pulsed laser

under different poling voltages was systematically investigated. As compared with the PDs based on the ferro–pyro–phototronic effect in BTO and NBT ceramics already described, this work presents a PD with a 3250-fold increase in responsivity and 35,000 and 36,000 times faster τ_r and τ_f, respectively. Compared to the Au/BCZT (700 nm)/Pt PD,[18] the present PD showed a 52 times increase in responsivity and 7 times higher detectivity. When compared with vertical multilayered $BiFeO_3/ZnTiO_3$ thin-film structures, our devices show 1.77 times higher responsivity and ~8300 times higher τ_r and τ_f.[19] Compared with other standard thin-film PDs, such as $Au/CH_3NH_3PbBr_3$/p-Si/Si, our devices show 4280 and 35,600 times faster τ_r and τ_f, respectively.[20]

Herein, we demonstrate the performance of a Al/Si/SiO_x/BCZT/ITO device structure, relating it to the structural and ferroelectric properties that give rise to a combined ferro–pyro–phototronic mechanism.

2 | EXPERIMENTAL METHODS

To grow the Al/Si/SiO_x/BCZT/ITO devices, an n-type BCZT film with a thickness of 80 nm was deposited using ion beam sputter deposition (IBSD) on n-type Si (100) substrates (Si-Mat). As described in our previous work, a 3 nm SiO_x native oxide layer exists at the n-Si/BCZT interface.[21] The BCZT layer was grown following the same procedure as that reported in our previous work[20,22] and by using a BCZT target prepared by a conventional solid-state reaction as previously described by Oliveira et al.[23] The vacuum chamber was first evacuated down to a low pressure of 1×10^{-6} mbar before the deposition. During the deposition, the substrate was maintained at a temperature of 330°C and at a distance of 87.3 mm from the target. The gas pressure inside the chamber was maintained constant at 2.5×10^{-4} mbar. A gas flow of 6.0 mL min^{-1} of Ar + 2.0 mL min^{-1} of O_2 was introduced into the ion beam gun and the atoms were ionized in the ion source with an rf-power of 120 W. The ion beam was further accelerated at 900 V and the ion beam current was regulated to remain at 31 mA. After the deposition, the BCZT film was annealed in air for 30 min, at 750°C, to reduce oxygen vacancies and associated carriers, and thus to reduce leakage.

The structural properties of the BCZT layer were investigated using grazing incidence X-ray diffraction (GIXRD) with a Bruker D8 Discover diffractometer using Cu–Kα radiation ($\lambda = 1.54056$ Å) and $\omega = 2.0°$ scanning electron microscopy (SEM) was used to investigate the morphology and cross-section of the BCZT layer, performed using an FEI NOVA NanoSEM 200.

To fabricate PDs, an indium tin oxide (ITO) top electrode with a size of 2×6 mm^2 and a thickness of 40 nm was deposited by IBSD as reported in Silve et al.,[24] while aluminum electrodes were attached to the back of a Si wafer by an electric spark. The current–time (I–t) characteristics were measured using a current amplifier Keithley 428 and National Instrument I/O card PCI-6251 programmed in Labview. The illumination of the devices was provided by the semiconductor laser with a wavelength of 405 nm and a power of 45.3 mW controlled with a TTL signal, which corresponds to a power density of 230 mW/cm^2. We applied a chopper frequency effect, using pulsed repetition rates of 50, 100, 200, 300, and 400 Hz. The poling was done by applying a voltage in the range from −15 to +15 V to the top ITO electrode using a Keithley 2601A source meter for 10 s. The ferroelectric hysteresis loops (P–V) were measured at room temperature with a modified Sawyer–Tower circuit using a sinusoidal signal at 1 kHz.

3 | RESULTS AND DISCUSSION

The structural characteristics of the n-Si/SiO_x/BCZT heterostructure were investigated by GIXRD. Figure 1A shows the XRD pattern of the n-Si/SiO_x/BCZT heterostructure. The crystallographic planes of diffraction peaks were successfully indexed according to the JCPDS file No.: 05-0626, 85-0368.[25] The pattern shows characteristic Bragg peaks of the perovskite tetragonal phase of BCZT,[21,26] without any secondary phases observed. Figure 1B shows a cross-sectional SEM image of the n-Si/SiO_x/BCZT heterostructure. The cross-sectional SEM image reveals the formation of a uniform and compact 80 ± 5 nm-thick BCZT layer. However, within the resolution of the equipment, it is not possible to observe the presence of the SiO_x layer between the Si substrate and the BCZT layer. The surface morphology of the BCZT layer is shown in Figure 1C, and confirms the uniformity and compactness of the BCZT layer with a granular structure. Given the low contents of Zr and Ca in the BCZT film, energy-dispersive X-ray spectroscopy is not sensitive enough to accurately determine all the elements present in the BCZT layer. However, we have previously used X-ray photoelectron spectroscopy[23] and scanning transmission electron microscopy with electron energy loss spectroscopy to map the elements[22] in the BCZT film.

The transient response characteristics of the Al/Si/SiO_x/BCZT/ITO device were investigated under zero bias, with 405 nm laser illumination, at a fixed power density of 230 mW/cm^2 and as a function of the pulse repetition rate. The device structure is shown in Figure 1D, and from the

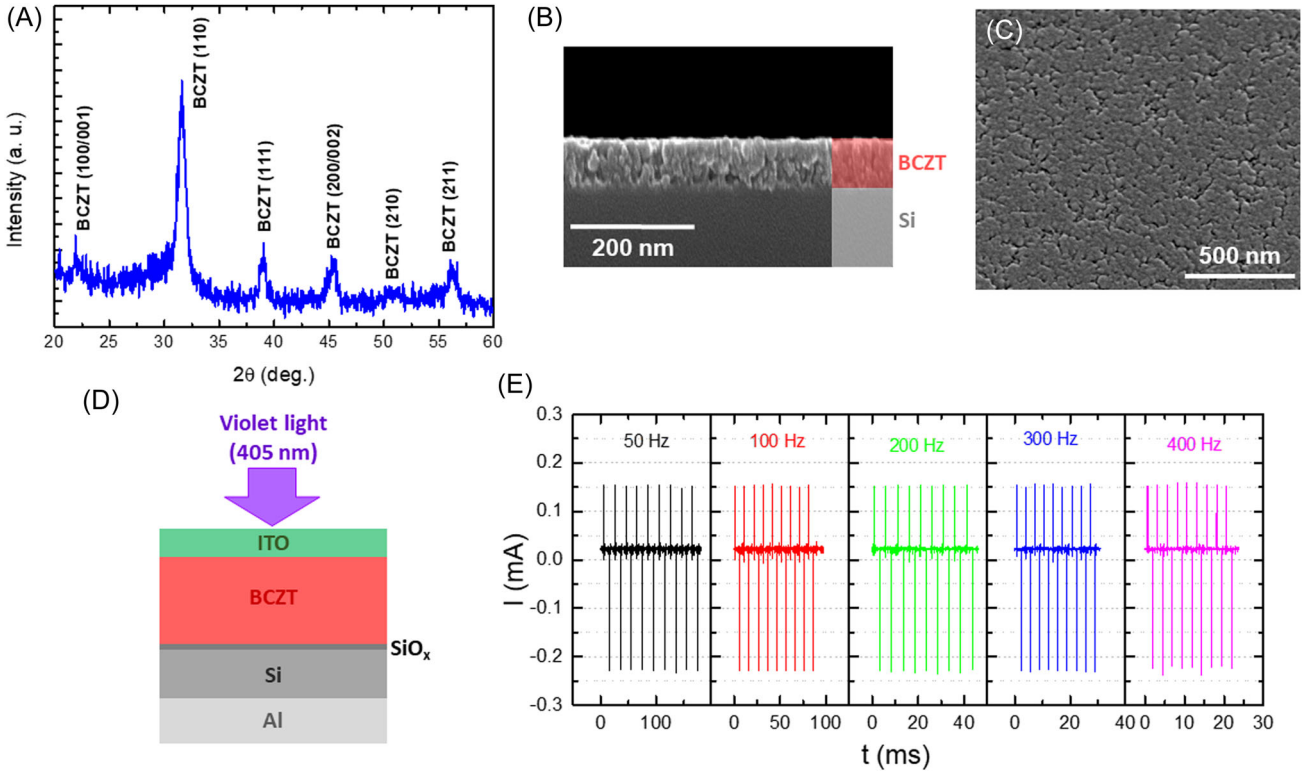

FIGURE 1 Structural, morphological, and electrical characterization of the heterostructure of Si/SiO_x/BCZT. (A) GIXRD pattern, (B) cross-sectional scanning electron micrograph, and (C) surface morphology of the BCZT layer. (D) Illustration of the device cross section and (E) *I*–*t* curves for the Al/Si/SiO_x/BCZT/ITO device at different chopper frequencies and at a fixed power density of 230 mW/cm^2. GIXRD, grazing incidence X-ray diffraction.

I–*t* curves shown in Figure 1E, one can conclude that the pyro–phototronic effect occurs and the typical photocurrent dynamic response is observed with stable characteristics. Furthermore, no significant differences were observed for the different pulsed repetition rates. This suggests that short pulses are enough to achieve the pyro–phototronic effect with the optimum characteristics. The pyro–phototronic effect can be described as follows[2,7,27]: in the beginning, there is a small dark current (I_{Dark}). On illumination with a 405 nm laser, a sharp current peak ($I_{Pyro+PV}$) occurs in a short period of time due to the coupling between the pyroelectric and photovoltaic effects, via the pyro–phototronic effect. Subsequently, under stable illumination, the temperature becomes constant and the light-induced temperature gradient disappears; therefore, the current decays from $I_{Pyro+PV}$ to I_{PV}. Although this current is hardly visible in this figure, it can be seen in Figure 5A. The bandgap of BCZT is ~3.12 eV (397 nm),[21] which is close to the violet laser source used in this work, and typically it shows a poor photovoltaic effect.[24] When the laser is turned off, the temperature gradient in the BCZT film appears in the opposite direction and therefore a reverse current spike flowing in the reverse direction emerges. In the end, the current returns back to I_{Dark}, since the reverse temperature gradient in the BCZT film disappears. The PD parameters such as responsivity (R), detectivity (D^*), and sensitivity (S) were estimated using the following equations[27,28]:

$$R = \frac{I_{Light} - I_{Dark}}{P}, \tag{1}$$

$$D^* = R\left(\frac{A}{2qI_{Dark}}\right)^{1/2}, \tag{2}$$

$$S = \frac{I_{Light} - I_{Dark}}{I_{Dark}}, \tag{3}$$

where I_{Light} and I_{Dark} are the short-circuit currents with and without illumination, respectively. P and A are the effective illumination power and area on the PD, respectively, and q represents the electron charge. The R, D^*, and S are equal to 3.3 mA/W, 4.3×10^9 Jones, and 6.8, respectively, without using any poling procedure.

To determine the role of the ferroelectric polarization of the BCZT film in the PD performance of the Al/Si/SiO_x/BCZT/ITO device, the transient response

characteristics were measured after the application of a poling voltage. Figure 2A,B shows the *I–t* curves after applying a poling voltage. From Figure 2, one can conclude that the poling voltage has a strong impact on the pyro–phototronic effect. Figure 2C shows a P–V loop confirming the ferroelectric nature of the Al/Si/SiO_x/BCZT/ITO device. A coercive voltage (*Vc*) of ~5 V was obtained with a saturation polarization (P_s) of 3.3 μC/cm^2 and a remnant polarization (P_r) of 1.5 μC/cm^2.

Figure 3 shows current (A), *R* (B), *D** (C), and *S* (D) as a function of poling voltage. The current in (A) is defined as $I_{FE+Pyro+PV}$ and it results from the combination of ferroelectric, pyroelectric, and photovoltaic effects. In Figure 3, we can observe irreversible loops; that is, from −15 to +15 V, the different parameters have values that are four times higher than that for +15 to −15 V.

Saturated hysteresis loop dependence of $I_{FE+Pyro+PV}$ and the other parameters as a function of the poling voltage is observed over quite a broad voltage range. The plots mimic Figure 2A,B, where saturation of current is observed in the middle band of voltages from ±1 V up to ±5 V. Then, the current increases from −6 V up to −15 V and tends to saturate, while it decreases from +6 V up to +15 V. These results can be understood as follows: at a low poling voltage (from ±1 V up to ±5 V), the initial ferroelectric polarization in the BCZT layer is weak, because the applied voltage is below the coercive voltage of the BCZT layer, as shown in the P–V loop of Figure 2C. Therefore, $I_{FE+Pyro+PV}$ does not show a significant variation. In Figure 2C, the circles and squares highlight the polarization at a voltage where a significant current change is observed in Figure 2A,B, respectively. It can be observed that the polarization highlighted by the circles changes marginally in the range −15 V up to −6 V, which corresponds to a slight decrease of the $I_{FE+Pyro+PV}$ in Figure 2A. However, it can be observed that the polarization changes significantly in the range +6 V up to +15 V, which corresponds to a significant decrease in $I_{FE+Pyro+PV}$. In the case of the polarization highlighted by the squares, it changes marginally in the range +6 V up to +15 V, which corresponds to a slight decrease in $I_{FE+Pyro+PV}$, while it decreases significantly in the range −15 V up to −6 V, which corresponds to a significant change in $I_{FE+Pyro+PV}$ in Figure 2B. To further understand the variation of current, *R*, *D**, and *S* as a function of poling voltage (Figures 2 and 3), and the role of the ferroelectric polarization in BCZT in the PD

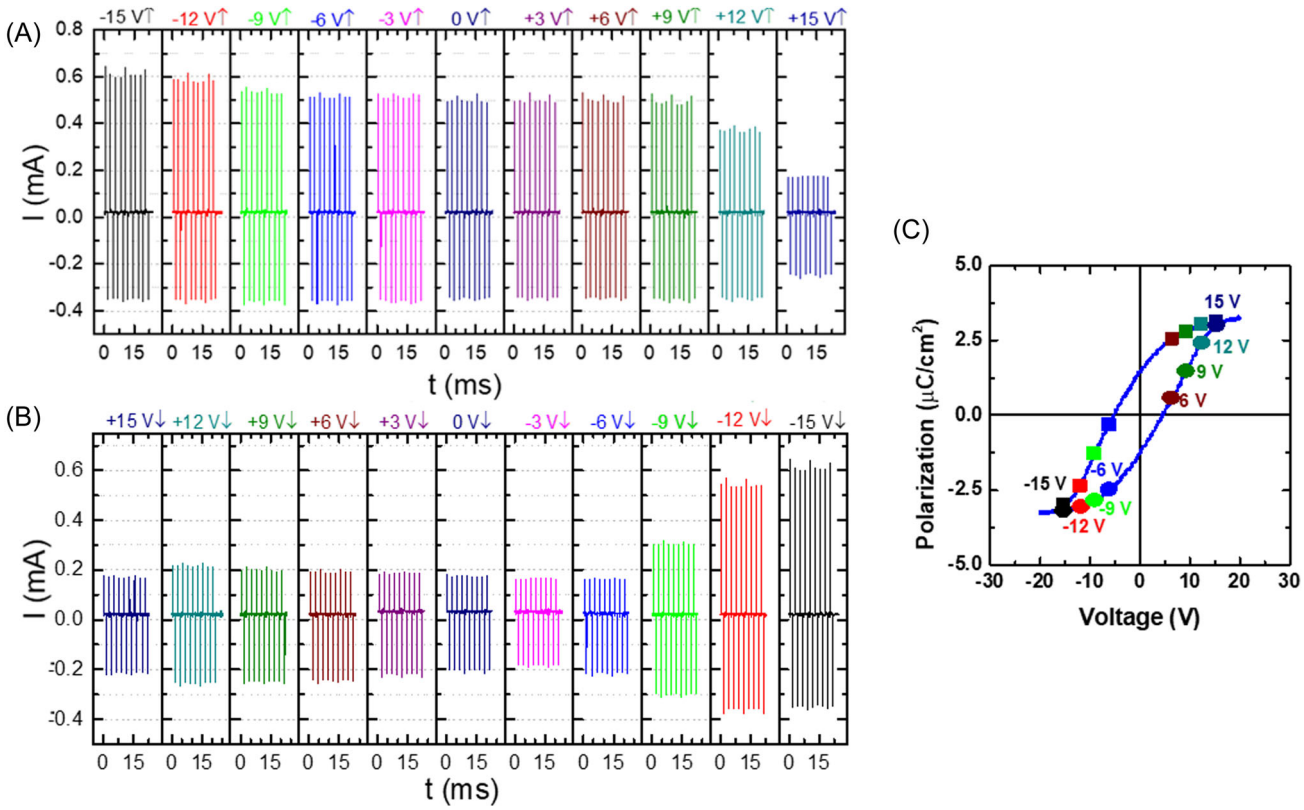

FIGURE 2 *I–t* curves for the Al/Si/SiO_x/BCZT/ITO device measured after different poling voltages and at a fixed chopper frequency of 400 Hz and a fixed power density of 230 mW/cm^2. (A) From −15 V up to +15 V and (B) from +15 V down to −15 V. (C) P–V loop for the Al/Si/SiO_x/BCZT/ITO device. Circles and squares highlight the polarization at a voltage where a significant current change is observed in (A) and (B), respectively.

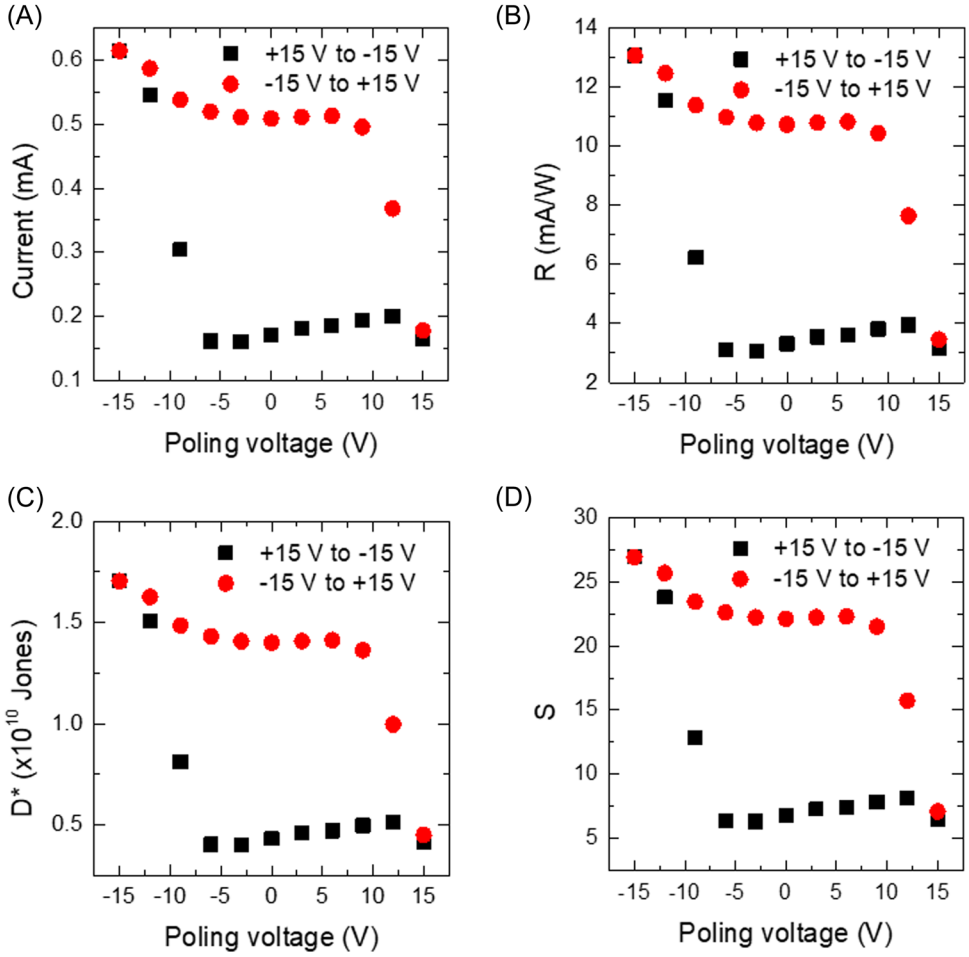

FIGURE 3 Variation of (A) current ($I_{FE+Pyro+PV}$), (B) responsivity (R), (C) detectivity (D^*), and (D) sensitivity (S) as a function of poling voltage.

performance in the ±6 V up to ±15 V range, we compare the energy band diagrams of the Al/Si/SiO_x/BCZT/ITO heterostructure for two typical polarization states. Immediately, after the violet light is turned on, a temperature gradient is established at the BCZT layer, as shown in Figure 4A,B. We consider the different internal fields, band levels, and current values when the device is illuminated. The energy band diagrams are valid for poling voltages ≥ ±6 V, where the coercive voltage is exceeded.

For both situations (i.e., either negative poling (Figure 4A) or positive poling (Figure 4B) field), there is a constant built-in field ($E_{bi\text{-}1}$) with the opposite sign between the ITO contact and the BCZT, and this produces a built-in electric field, $E_{bi\text{-}1}$. When the device is illuminated (and heated), there is also a constant pyroelectric electric field (E_{Pyro}) across the BCZT film that points toward the Si substrate. Two other built-in fields are present, and the signs of these are opposite for the two cases of negative poling (positive poling field).

First, there is the depolarization field, $E_{dp\text{-}BCZT}$, which opposes the ferroelectric polarization direction. Second, there is the built-in electric field ($E_{bi\text{-}2}$) at the BCZT/SiO_x/n-Si heterojunction due to the bandgap and carrier concentration difference at this interface.

After a negative poling voltage (≤−6V), in excess of Vc (Figure 4A), the direction of the ferroelectric polarization causes the barrier height/width to increase at the ITO/BCZT interface and upward band bending is induced in BCZT. Also, there is an upward band bending in Si because of the presence of an electric field at the junction between Si and BCZT. Both these fields oppose the movement of the carriers. Hence, with a negative poling voltage, $E_{dp\text{-}BCZT}$ and E_{Pyro} are aligned in the same direction in the Al/Si/SiO_x/BCZT/ITO device and this leads to a higher $I_{FE+Pyro+PV}$ compared to the one observed after a poling voltage from ±1 V up ±5 V, where $E_{dp\text{-}BCZT}$ is negligible. This explains the high saturation current observed in Figure 2A at −15 V and the high values of the three PD parameters in Figure 3.

After a positive poling voltage (≥+6 V), in excess of Vc, the ferroelectric polarization is reversed and thus all the internal fields are in the same direction, except for

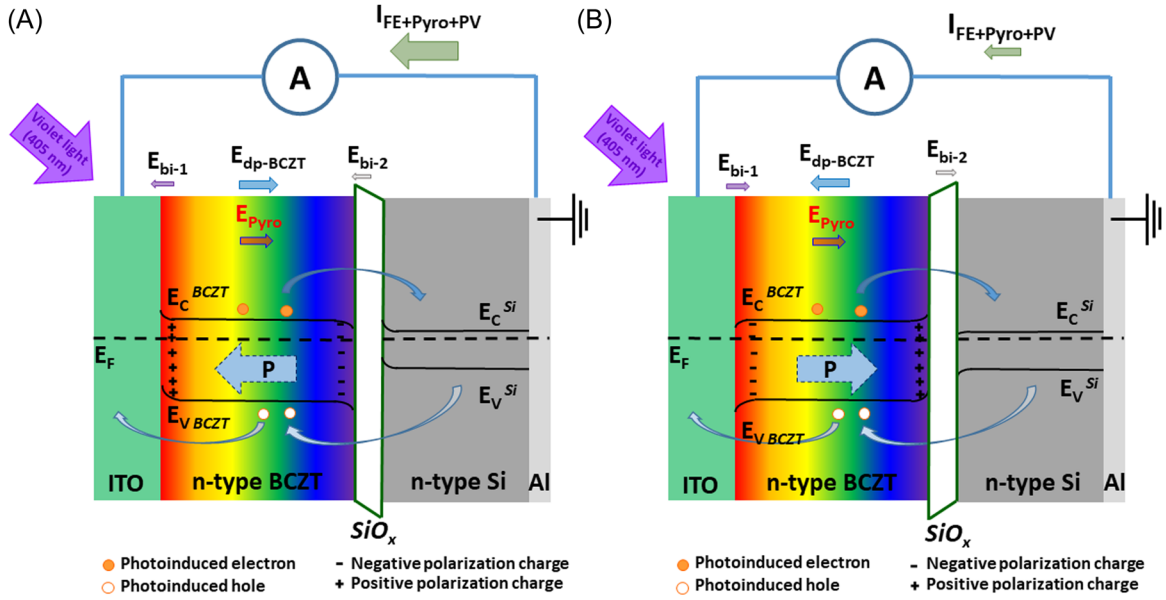

FIGURE 4 Schematic energy band diagrams and internal electric field distribution and the generation, separation, and motion of photo-induced carriers through the ferro–pyro–phototronic effect in the Al/Si/SiO_x/BCZT/ITO device in opposite polarization conditions of the BCZT layer for (A) negative poling voltage and (B) positive poling voltage. The sizes of the arrows are schematically related to the field strengths. The photo-induced carrier (electrons and holes) movement is shown schematically using blue arrows to depict their direction.

$E_{dp\text{-BCZT}}$. It is worth mentioning that the saturation in the P–V loop (Figure 2C) is reached at ±15 V, which is close to the saturation observed in the *I–t* measurements (Figure 2A,B). Furthermore, after a positive poling voltage (≥+6 V), in excess of *Vc* (Figure 4B), the direction of the ferroelectric polarization causes the barrier height/width to decrease at the ITO/BCZT interface and thus downward band bending is induced in BCZT. Also, there is a downward band bending in Si because of the opposite direction of the electric field at the junction between Si and BCZT. These two fields, together with E_{Pyro}, promote carrier movement. However, with a positive poling voltage, $E_{dp\text{-BCZT}}$ is opposite in the Al/Si/SiO_x/BCZT/ITO device and this leads to a reduction of $I_{FE+Pyro+PV}$ compared with the one observed after a poling voltage from ±1 V up ±5 V, where $E_{dp\text{-BCZT}}$ is negligible. This explains the saturation current observed in Figure 2B at +15 V and PD parameters in Figure 3, where the magnitude of $E_{dp\text{-BCZT}}$ seems to be higher than those of the other fields. This indicates that polarization-dependent interfacial coupling between ITO and BCZT and between BCZT and SiO_x/Si highly influences the band diagram of the heterostructure including the potential barrier height. The work is consistent with previous studies that showed that the interface band diagrams in ferroelectrics such as BCZT or $Pb(Zr,Ti)O_3$ change with the poling voltage.[24,29] Thus, the data of Figures 2 and 3 can be explained by both the magnitude of the overall field that drives the current as well as the band structure modulation arising from the ferro–pyro–phototronic effect.

The *R*, *D**, and *S* parameters were estimated as a function of the poling voltage and are shown in Figure 3B–D. As expected, a similar butterfly-shaped behavior is observed in the *R, D**, and *S* parameters similar to what was observed for $I_{FE+Pyro+PV}$ (Figure 3A). Maximum *R, D**, and *S* parameters were achieved with a poling voltage of −15 V and are equal to 13.1 mA/W, 1.7×10^{10} Jones, and 26.9, respectively, which correspond to an increase in the *R, D**, and *S* parameters by almost four times when compared with the device performance without any poling voltage.

Figure 5A shows a representative transient characteristic of the device in response to an ON/OFF cycle under violet laser irradiation measured with a laser power density of 230 mW/cm^2 and with a chopper frequency of 400 Hz. $I_{FE+Pyro+PV}$, $I_{FE+Pyro}$, and I_{PV} are also represented. The $I_{Pyro+PV}$ shown in Figure 1E is also marked by a dashed orange line for comparison. The τ_r at the rising edge and τ_f at the falling edge values were also calculated following the procedure described by Wang and colleagues[1,21], and are equal to 2.4 and 1.5 μs, respectively. Similar values of τ_r and τ_f were obtained in the transient response when the laser was turned ON or OFF. Figure 5B shows the stability of the transient response characteristics of the Al/Si/SiO_x/BCZT/ITO device under zero bias and with 405 nm laser illumination and a laser power density of 230 mW/cm^2. It can be

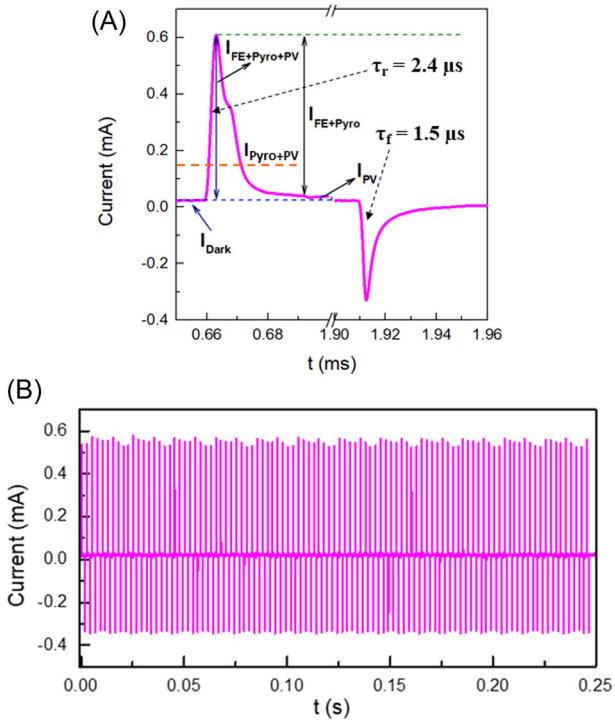

FIGURE 5 (A) A typical transient response of the device with 405 nm laser illumination. $I_{FE+Pyro+PV}$, $I_{FE+Pyro}$, and I_{PV} are represented in the figure. The $I_{Pyro+PV}$ achieved in Figure 1E is also marked by a dashed orange line for comparison. (B) Stability of the transient response characteristics of the Al/Si/SiO_x/BCZT/ITO device after a poling voltage of −15 V and with 405 nm laser illumination and a laser power density of 230 mW/cm^2.

observed that the PD shows a stable response up to 100 cycles, without a degradation of the performance.

Table 1 shows a comparison between the *R*, *D**, τ_r, and τ_f of the PDs obtained in this work with the ones presented in the recent literature based on the ferro–pyro–phototronic effect in ferroelectric oxides or the pyro–phototronic effect for UV-Vis photodetection. The present PDs show outstanding responsivity and detectivity, and the ultrafast fall and rise times make them the most promising PDs to date based on the ferro–pyro–phototronic effect. In addition, the PDs based on the ferro–pyro–phototronic devices presented in Table 1 are from bulk BTO and BNT ceramics, while the present ones are based on BCZT thin films with a reduction in thickness of ~250 times. The excellent improvement of the fall and rise times arises from the use of a BCZT thin-film device instead of bulk BTO and BNT ceramic devices, leading to a faster and larger light-induced temperature gradient and consequently a faster response time. In terms of the ZnO-based PDs achieved through the pyro-phototronic effect, the present devices show comparable responsivity and detectivity, and they show 250 and 330 times faster rise and fall responses. However, PDs based on ZnO heterostructures usually show improved performance with regard to response times. Compared with the best thin-film devices based on ZnO/SnO_x bilayered devices achieved through the pyro–phototronic effect, the present PD still, respectively, shows 1.25 and 1.33 times faster rise and fall responses. Besides, multilayered thin films usually introduce complexity to the fabrication process and SnO_x layers, composed of SnO and SnO_2, are susceptible to oxidation reactions, degrading the PD performance with cycling. We envisage that the use of ZnO materials in addition to the ferro/pyroelectric materials studied here, to create a ferroelectric–semiconductor heterostructure of BCZT/ZnO, will further improve the PD performance of our single thin-film ferroelectric heterostructure device.

We note that planar PDs based on the ferro–pyro–phototronic effect have also been investigated for UV photodetection, that is, Ag/Bi/2D PMA_2PbCl_4/Bi/Ag PDs, where PMA_2PbCl_4 ((benzylammonium)$_2PbCl_4$) is a 2D ferroelectric material and Bi/Ag are electrodes. This system show a high *R* and *D** up to 9 A/W and 1.01×10^{11} Jones, respectively, under 320 nm laser illumination. However, this system uses more complex processing (e.g., patterning); the PDs show a slow rise time and fall time of 162 and 226 µs, respectively.[3] There are questions over long-term stability and toxicity of the PMA_2PbCl_4. Moreover, two-dimensional Ruddlesden–Popper-layered metal–halide perovskites are also being investigated for PDs[30-32] and they can show excellent $R > 16$ A/W and $D^* > 3 \times 10^{13}$ Jones. However, the response time is quite slow, on the order of 10 ms. In addition, the complex growth process of single-crystal membranes and uncontrollable phase distribution of polycrystalline films hinder further development of these PDs. On the other hand, PDs based on $CsPbBr_3$ NWs show a high responsivity of 5.49 A/W, with slow rise and fall times of 95 and 40 ms, respectively.[33] Overall, considering all the performance parameters and practicality aspects of currents PDs, that is, ferroelectric- and ZnO-based PDs, our PDs exceed these in terms of the combination of critical performance parameters, ease of processing of materials, relatively benign composition, and stability.

4 | CONCLUSION

A novel Al/Si/SiO_x/BCZT/ITO PD device was fabricated by ion beam sputtering. The poling voltage had a strong impact on the photocurrent, responsivity, detectivity, and sensitivity of the device, indicative of the importance of the ferroelectric effect in BCZT for enhancing the pyro–phototronic effect. The responsivity, detectivity, and sensitivity of the device to violet light are increased almost

TABLE 1 Comparison of the R, D^*, τ_r, and τ_f obtained in this work with the ones presented in the literature for UV-Vis PDs

Device	Thickness (nm)	Power density (mW/cm^2)	Wavelength (nm)	R (mA/W)	D^* (Jones)	τ_r (μs)	τ_f (μs)	Ref.
Ferro–pyro–phototronic effect in ferroelectric oxide PDs								
$ITO/BaTiO_3/ITO$	8.5×10^5	131	405	1.4×10^{-3}	1.5×10^7	-	-	[10]
$Ag/BaTiO_3/ITO$	1.98×10^4	7.8	405	7.5×10^{-3}	2×10^9	9×10^5	1×10^6	[11]
$Ag/Bi_{0.5}Na_{0.5}TiO_3/ITO$	3×10^5	156	405	4.1×10^{-3}	1.3×10^7	8.4×10^4	5.4×10^4	[12]
$Al/Si/SiO_x/BCZT/ITO$	80	230	405	13.1	1.7×10^{10}	2.4	1.5	This work
Pyro–phototronic effect in ZnO-based PDs								
PET/ITO/ZnO/Ag	1×10^3	0.01	325	1.25	2.7×10^9	2500	1200	[1]
Ag/Si/ZnO/ITO	600	0.03	325	0.7	2.2×10^9	700	400	[6]
Ag/Si/ZnO/ITO	600	0.015	442	79.9	2.5×10^{10}	600	500	[6]
Ag/Si/ZnO/ITO	600	0.34	633	17.9	6.4×10^9	900	700	[6]
$ITO/V_2O_5/ZnO/ITO$	125	4	365	36	6×10^{14}	4	16	[30]
$Al/Si/SnO_x/ZnO/ITO$	75	36.3	405	36.7	1.5×10^{11}	2	1	[27]

Abbreviations: PD, photodetector; UV, ultraviolet; Vis, visible.

four times when comparing poled and unpoled BCZT for a poling voltage of −15 V over a BCZT film of 80 nm thickness. These results are understood based on the ferro–pyro–phototronic effect, where the polarization-dependent interfacial coupling can greatly influence the magnitude of the combined pyroelectric and photovoltaic generated current. Thus, the polarization field influences both the overall field to drive carrier extraction and the band bending at the electrode interfaces with the BCZT, influencing how easily the carriers can be extracted at the electrodes. Ultrafast rise and fall times of 2.4 and 13.0 μs were obtained, respectively, which are by far the fastest devices based on the ferro–pyro–phototronic effect to date. The photoresponse performance was not influenced by chopper frequency. Overall, our work demonstrates a very promising ultrafast PD for violet light based on a stable thin-film inorganic perovskite oxide ferroelectric material that also exploits its photovoltaic and pyroelectric effects in a metal–ferroelectric–insulator–semiconductor heterostructure. The ferroelectric effect is shown to enhance the PD performance by a factor of 4.

ACKNOWLEDGMENTS

This work was supported by the Portuguese Foundation for Science and Technology (FCT) in the framework of the Strategic Funding Contracts UIDB/04650/2020. This project has received funding from the European Union's Horizon 2020 research and innovation program under grant agreement No 958174 (M-ERA-NET3/0003/2021—NanOx4EStor). The authors would also like to thank engineer José Santos for technical support at the Thin Film Laboratory. J. L. M.-D. and R. L. Z. H. are grateful for EPSRC CAM-IES grant EP/P007767/. R. L. Z. H. also acknowledges support from the Royal Academy of Engineering under the Research Fellowships scheme (No.: RF\201718\1701). J. L. M.-D. acknowledges support from the Royal Academy of Engineering Chair in Emerging Technologies scheme (No.: CIET1819_24) and the ERC grant EROS, EU-H2020-ERC-ADG # 882929.

CONFLICTS OF INTEREST

The authors declare no conflicts of interest.

ORCID

José P. B. Silva http://orcid.org/0000-0002-3485-7032

REFERENCES

1. Wang Y, Zhu L, Feng Y, Wang Z, Wang ZL. Comprehensive pyro-phototronic effect enhanced ultraviolet detector with ZnO/Ag Schottky junction. *Adv Funct Mater*. 2019;29(5):1807111.
2. Peng W, Pan Z, Li F, Cai Y, He Y. Pyro-phototronic effect enhanced ZnO nanowire-based tri-layer heterojunction for visible light sensing and communication. *Nano Energy*. 2020;78:105268.
3. Guo L, Liu X, Gao L, et al. Ferro-pyro-phototronic effect in monocrystalline 2D ferroelectric perovskite for high-sensitive, self-powered, and stable ultraviolet photodetector. *ACS Nano*. 2022;16(1):1280-1290.
4. Ouyang W, Chen J, Shi Z, Fang X. Self-powered UV photodetectors based on ZnO nanomaterials. *Appl Phys Rev*. 2021;8(3):031315.
5. Wang Z, Yu R, Pan C, et al. Light-induced pyroelectric effect as an effective approach for ultrafast ultraviolet nanosensing. *Nat Commun*. 2015;6:8401.

6. Zhang Y, Hu M, Wang Z. Enhanced performances of p-si/n-ZnO self-powered photodetector by interface state modification and pyro-phototronic effect. *Nano Energy*. 2020;71:104630.
7. Wang Z, Yu R, Wang X, Wu W, Wang ZL. Ultrafast response p-Si/n-ZnO heterojunction ultraviolet detector based on pyro-phototronic effect. *Adv Mater*. 2016;28(32):6880-6886.
8. Zhao K, Ouyang B, Yang Y. Enhancing photocurrent of radially polarized ferroelectric $BaTiO_3$ materials by ferro-pyro-phototronic effect. *iScience*. 2018;3:208-216.
9. Zhao K, Ouyang B, Bowen CR, Wang ZL, Yang Y. One-structure-based multi-effects coupled nanogenerators for flexible and self-powered multi-functional coupled sensor systems. *Nano Energy*. 2020;71:104632-4320.
10. Ma N, Yang Y. Boosted photocurrent via cooling ferroelectric $BaTiO_3$ materials for self-powered 405 nm light detection. *Nano Energy*. 2019;60:95-102.
11. Zhao K, Ouyang B, Bowen CR, Yang Y. Enhanced photocurrent via ferro-pyro-phototronic effect in ferroelectric $BaTiO_3$ materials for a self-powered flexible photodetector system. *Nano Energy*. 2020;77:105152.
12. Liu Y, Ji Y, Xia Y, Wu L, Bowen CR, Yang Y. Enhanced photocurrent in ferroelectric $Bi_{0.5}Na_{0.5}TiO_3$ materials via ferro-pyro-phototronic effect. *Nano Energy*. 2022;98:107312.
13. Silva JPB, Queirós EC, Tavares PB, et al. Ferroelectric phase transitions studies in $0.5Ba(Zr_{0.2}Ti_{0.8})O_3$-$0.5(Ba_{0.7}Ca_{0.3})TiO_3$ ceramics. *J Electroceram*. 2015;35(1-4):135-140.
14. Lente MH, Araújo EB. Kinetics of reorientation ferroelectric polarisation in PZT bulk ceramics and thin films. *Ferroelectrics*. 2000;238(1):73-80.
15. Silva JPB, Kamakshi K, Negrea RF, et al. Ferroelectric switching dynamics in $0.5Ba(Zr_{0.2}Ti_{0.8})O_3$-$0.5(Ba_{0.7}Ca_{0.3})TiO_3$ thin films. *Appl Phys Lett*. 2018;113(8):082903.
16. Tagantsev AK, Stolichnov I, Setter N, Cross JS, Tsukada M. Non-Kolmogorov-Avrami switching kinetics in ferroelectric thin films. *Phys Rev B*. 2002;66(21):214109.
17. Shi C, Yan F, Ge G, Wei Y, Zhai J, Yao W. Significantly enhanced energy storage performances and power density in (1−x)BCZT-xSBT lead-free ceramics via synergistic optimization strategy. *Chem Eng J*. 2021;426:130800.
18. Swain AB, Rath M, Biswas PP, Rao MSR, Murugavel P. Polarization controlled photovoltaic and self-powered photodetector characteristics in Pb-free ferroelectric thin film. *APL Mater*. 2019;7(1):011106.
19. Li S, Wang L, Zhang J, et al. A self-powered flexible UV-visible photodetector with high photosensitivity based on $BiFeO_3$/$XTiO_3$ (Sr, Zn, Pb) multilayer films. *J Mater Chem A*. 2022;10(16):8772-8783.
20. Yang S, Chen M, Shen X, et al. Self-powered narrowband visible-light photodetection enabled by organolead halide perovskite $CH_3NH_3PbBr_3$/p-Si heterojunction. *Appl Phys Lett*. 2021;119(12):121107.
21. Silva JPB, Vieira EMF, Silva JMB, et al. Perovskite ferroelectric thin film as an efficient interface to enhance the photovoltaic characteristics of Si/SnO_x heterojunctions. *J Mater Chem A*. 2020;8(22):11314-11326.
22. Silva JPB, Sekhar KC, Veltruská K, et al. HfO_2–Al_2O_3 dielectric layer for a performing metal–ferroelectric–insulator–semiconductor structure with a ferroelectric $0.5Ba(Zr_{0.2}Ti_{0.8})O_3$-$0.5(Ba_{0.7}Ca_{0.3})TiO_3$ thin film. *ACS Appl Electron Mater*. 2020;2(9):2780-2787.
23. Oliveira MJS, Silva JPB, Veltruská K, et al. Annealing induced effect on the physical properties of ion-beam sputtered $0.5Ba(Zr_{0.2}Ti_{0.8})O_3$-$0.5(Ba_{0.7}Ca_{0.3})TiO_{3-\delta}$ ferroelectric thin films. *Appl Surf Sci*. 2018;443:354-360.
24. Silva JPB, Sekhar KC, Cortés-Juan F, et al. Ferroelectric photovoltaic characteristics of pulsed laser deposited $0.5Ba(Zr_{0.2}Ti_{0.8})O_3$-$0.5(Ba_{0.7}Ca_{0.3})TiO_3$/ZnO heterostructures. *Sol Energy*. 2018;167:18-23.
25. Jayakrishnan AR, Alex KV, Thomas A, et al. Composition-dependent $xBa(Zr_{30.2}Ti_{30.8})$ O_3-$(1-x)(Ba0_{0.7}Ca_{0.3})$ TiO_3 bulk ceramics for high energy storage applications. *Ceram Int*. 2019;45(5):5808-5818.
26. Silva JPB, Silva JMB, Oliveira MJS, et al. High-performance ferroelectric–dielectric multilayered thin films for energy storage capacitors. *Adv Funct Mater*. 2019;29(6):1807196.
27. Silva JPB, Vieira EMF, Gwozdz K, et al. High-performance self-powered photodetectors achieved through the pyro-phototronic effect in Si/SnO_x/ZnO heterojunctions. *Nano Energy*. 2021;89(Part A):106347.
28. Chen L, Wang B, Dong J, et al. Insights into the pyro-phototronic effect in p-Si/n-ZnO nanowires heterojunction toward high-performance near-infrared photosensing. *Nano Energy*. 2020;78:105260.
29. Pan D-F, Bi G-F, Chen G-Y, et al. Polarization-dependent interfacial coupling modulation of ferroelectric photovoltaic effect in PZT-ZnO heterostructures. *Sci Rep*. 2016;6:22948.
30. Kumar M, Patel M, Nguyen TT, Kim J, Yi J. High-performing ultrafast transparent photodetector governed by the pyro–phototronic effect. *Nanoscale*. 2018;10(15):6928-6935.
31. Liang C, Gu H, Xia J, et al. High-performance flexible perovskite photodetectors based on single-crystal-like two-dimensional Ruddlesden–Popper thin films. *Carbon Energy*. In press; doi:10.1002/cey2.251
32. Pan S, Zou H, Wang, AC, et al. Rapid capillary-assisted solution printing of perovskite nanowire arrays enables scalable production of photodetectors. *Angew Chem Int Ed*. 2020;59(35):14942-14949.
33. Liang C, Gu H, Xia Y, et al. Two-dimensional Ruddlesden–Popper layered perovskite solar cells based on phase-pure thin films. *Nat Energy*. 2021;6(1):38-45.

How to cite this article: Silva JPB, Gwozdz K, Marques LS, et al. Large ferro–pyro–phototronic effect in $0.5Ba(Zr_{0.2}Ti_{0.8})O_3$–$0.5(Ba_{0.7}Ca_{0.3})TiO_3$ thin films integrated on silicon for photodetection. *Carbon Energy*. 2022;1-10. doi:10.1002/cey2.297